ACS Catalysis

Research Article

Cite This: ACS Catal. 2018, 8, 2824−2832

pubs.acs.org/acscatalysis

Microporous Framework Induced Synthesis of Single-Atom Dispersed Fe-N-C Acidic ORR Catalyst and Its in Situ Reduced Fe-N_4 Active Site Identification Revealed by X-ray Absorption Spectroscopy

Meiling Xiao,[†] Jianbing Zhu,[†] Liang Ma,[‡] Zhao Jin,[§] Junjie Ge,[*,§] Xin Deng,[∥] Yang Hou,[∥] Qinggang He,[*,∥] Jingkun Li,[⊥] Qingying Jia,[⊥] Sanjeev Mukerjee,[⊥] Ruoou Yang,[#] Zheng Jiang,[#] Dangsheng Su,[&] Changpeng Liu,[§] and Wei Xing[*,†]

[†]State Key Laboratory of Electroanalytical Chemistry, Changchun Institute of Applied Chemistry, Chinese Academy of Sciences, Changchun 130022, People's Republic of China

[‡]Faculty of Materials Science and Chemistry, China University of Geosciences, Wuhan 430074, People's Republic of China

[§]Laboratory of Advanced Power Sources, Changchun Institute of Applied Chemistry, Chinese Academy of Sciences, Changchun 130022, People's Republic of China

[∥]College of Chemical and Biological Engineering, Zhejiang University, Hangzhou, Zhejiang 310027, People's Republic of China

[⊥]Department of Chemistry and Chemical Biology, Northeastern University, 360 Huntington Avenue, Boston, Massachusetts 02115, United States

[#]Shanghai Synchrotron Radiation Facility, Shanghai Institute of Applied Physics, Chinese Academy of Sciences, Shanghai 201204, People's Republic of China

[&]Shenyang National Laboratory for Material Science, Institute of Metal Research, Chinese Academy of Sciences, Shenyang, People's Republic of China

Supporting Information

ABSTRACT: Developing highly efficient, low-cost oxygen reduction catalysts, especially in acidic medium, is of significance toward fuel cell commercialization. Although pyrolyzed Fe-N-C catalysts have been regarded as alternatives to platinum-based catalytic materials, further improvement requires precise control of the Fe-N_x structure at the molecular level and a comprehensive understanding of catalytic site structure and the ORR mechanism on these materials. In this report, we present a microporous metal−organic-framework-confined strategy toward the preferable formation of single-atom dispersed catalysts. The onset potential for Fe-N-C is 0.92 V, comparable to that of Pt/C and outperforming most noble-metal-free catalysts ever reported. A high-spin Fe^{3+}-N_4 configuration is revealed by the ^{57}Fe Mössbauer spectrum and X-ray absorption spectroscopy for Fe L-edge, which will convert to Fe^{2+}-N_4 at low potential. The in situ reduced Fe^{2+}-N_4 moiety from high-spin O_x-Fe^{3+}-N_4 contributes to most of the ORR activity due to its high turnover frequency (TOF) of ca. 1.71 e s^{-1} $sites^{-1}$.

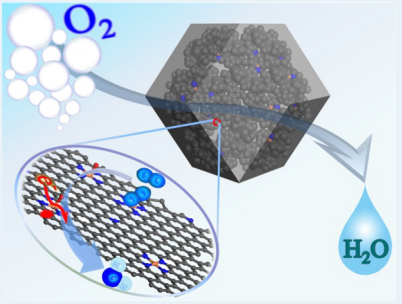

KEYWORDS: *oxygen reduction reaction, single atom, electrocatalyst, active site, X-ray absorption spectroscopy*

INTRODUCTION

Efficient synthesis and implementation of non-platinum-group-metal (non-PGM) catalysts toward the oxygen reduction reaction (ORR) is highly desirable but challenging for chemical energy conversion and storage.[1−4] Pyrolyzed metal−nitrogen−carbon catalysts (M-N_x-C, M = Co, Fe) are regarded as the most promising candidates, initiated by using cobalt phthalocyanine as an ORR catalyst in 1964.[5] Later, researchers recognized that the activity and durability in acidic solution can be largely enhanced by heat treatment.[6−8] In addition to metal−nitrogen-coordinated macrocycles, inorganic metal salts, nitrogen-containing polymers (polyaniline, polypyrrole) or small molecules (NH_3, melamine), and carbon black were selected as pyrolysis precursors for the synthesis of the M-N_x-C catalysts.[4,9−20] Significant breakthroughs in ORR performance using nonmacrocycle precursors to prepare the Fe-N_x-C catalysts were reported by Dodelet et al.[4] and Zelenay et al.[9] However, current progress primarily involves pyrolysis conditions and precursor optimization to maximize the performance.[21−26] The lack of a precise control strategy for the synthesis of catalyst and ongoing debate on the real active site structure have seriously limited further progress. The debate is associated with whether the transition metal participates in the ORR process.[27−33] Although most of the

Received: January 11, 2018
Revised: February 21, 2018
Published: February 21, 2018

DOI: 10.1021/acscatal.8b00138
ACS Catal. 2018, 8, 2824−2832

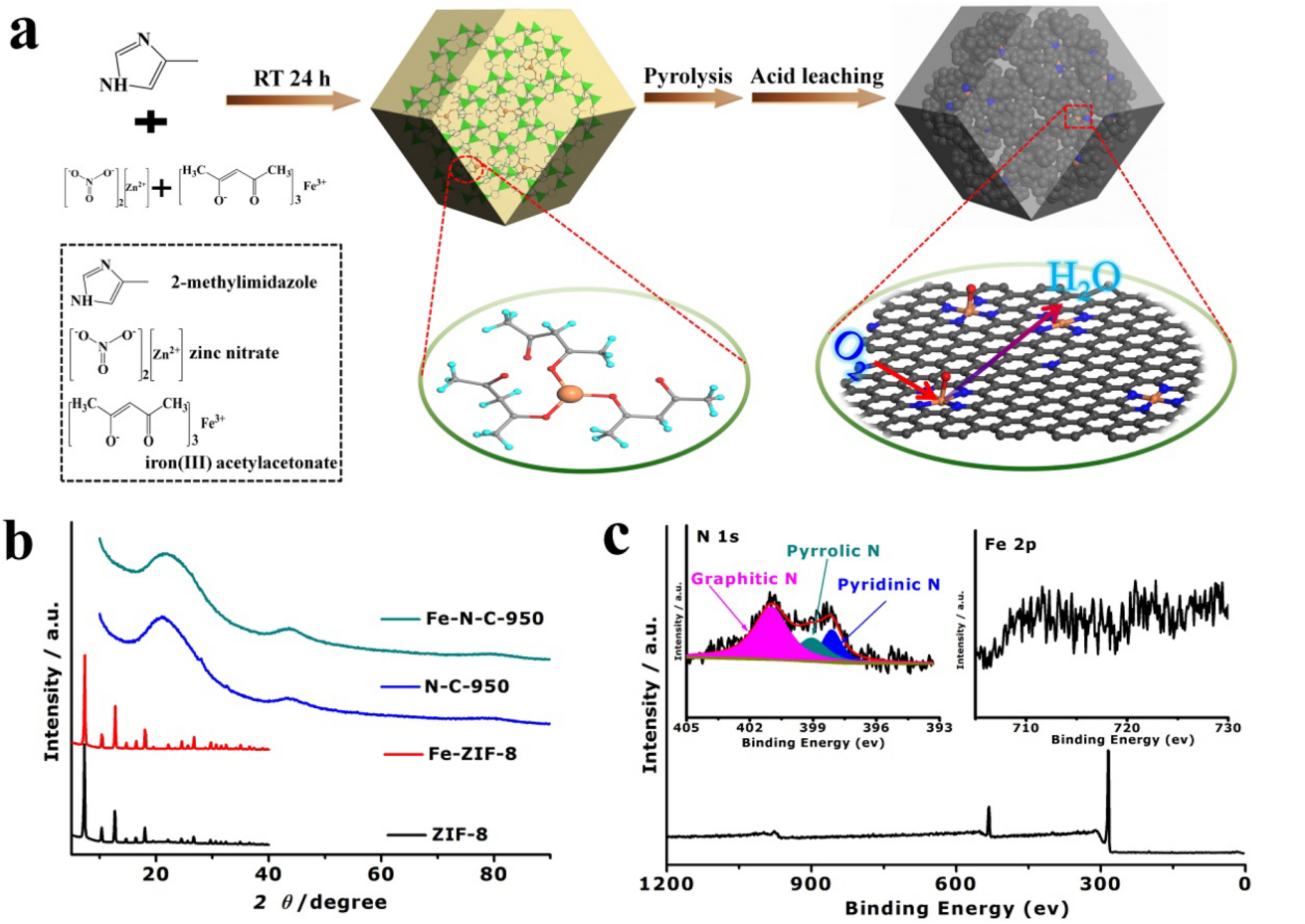

Figure 1. (a) Schematic procedure for the synthesis of Fe-N-C electrocatalysts. (b) XRD curves for ZIF precursors and carbonized samples. (c) XPS spectra of Fe-N-C-950 (inset: high-resolution N 1s and Fe 2p spectra).

literature claims that the active site is the M-N_x-C structure rather than a metal-free active site (N_x-C), the configuration of the M-N_x-C structures, including the coordination number and the electronic state of M, are still under extensive debate.[34−40] Moreover, the sintering process also induces the formation of crystalline metal particles, even at a low metal content, further complicating the identification of the real active site. Consequently, precise control of the material structure at an atomic level and the application of sophisticated structural analysis techniques, especially in situ spectroscopy, are urgently required to promote the development of non-PGM catalysts.

The typical procedure for synthesizing Fe-N-C catalysts consists of precursor mixing and pyrolyzing steps.[4,41−49] However, this method is time consuming and inevitably leads to catalysts with nonuniform structure. Metal−organic framework (MOF) materials with a large Brunauer−Emmett−Teller (BET) surface and highly porous structure are promising candidates for synthesizing efficient NPMCs. The abundant pores in MOF can serve as the host of the Fe precursor, thus promoting the dispersion and formation of the active Fe-containing phases. In our study, a microporous MOF-confined strategy was developed to synthesisize single-atom dispersed Fe-N-C material as a model catalyst. The Fe-N-C catalyst far exceeds the N-C species in catalyzing the ORR, although the latter possessed higher nitrogen content than the former, demonstrating the dominant role of the Fe-N_x active site over N_x-C species. The single-atom dispersion of Fe was confirmed by aberration-corrected scanning transmission electron microscopy (STEM) observations, ^{57}Fe Mössbauer spectroscopy, and extended X-ray absorption fine structure (EXAFS) spectra. The Fe coordination environment was studied by ^{57}Fe Mössbauer spectroscopy, with D1 (low-spin Fe^{2+}-N_4) and D2 (medium-spin Fe^{2+}-N_4 or high-spin O_x-Fe^{3+}-N_4) clearly observed. The discrepancies over the assignment of D2 were addressed by using X-ray absorption near edge structure (XANES) spectra of the Fe L-edge, which revealed the high-spin O_x-Fe^{3+}-N_4 configuration. To further identify the real active site structure, we conducted in situ XANES spectroscopy studies. The accompanying dynamic process of O_x-Fe^{3+}-N_4 switching to HO-*Fe($^{2+}$)-N_4 during the ORR was observed, which lowered the reaction barrier; therefore, higher a TOF value was obtained for the reduced Fe^{2+}-N_4 species. Our finding is of significant importance for the rational design of non-PGM catalysts in the future.

EXPERIMENTAL SECTION

Synthesis of ZIF-8 and Fe-ZIF-8. All syntheses were conducted at room temperature. Typically, 6.5 g of 2-methylimidazole (with 0.44 g of $Fe(acac)_3$ for Fe-ZIF-8) was dissolved in 80 mL of methanol with stirring. Then 40 mL of methanol containing 3 g of $Zn(NO_3)_2{\cdot}6H_2O$ was added with vigorous stirring for 24 h. The obtained product was centrifuged with methanol for several times and then dried at 60 °C under vacuum overnight.

DOI: 10.1021/acscatal.8b00138
ACS Catal. 2018, 8, 2824−2832

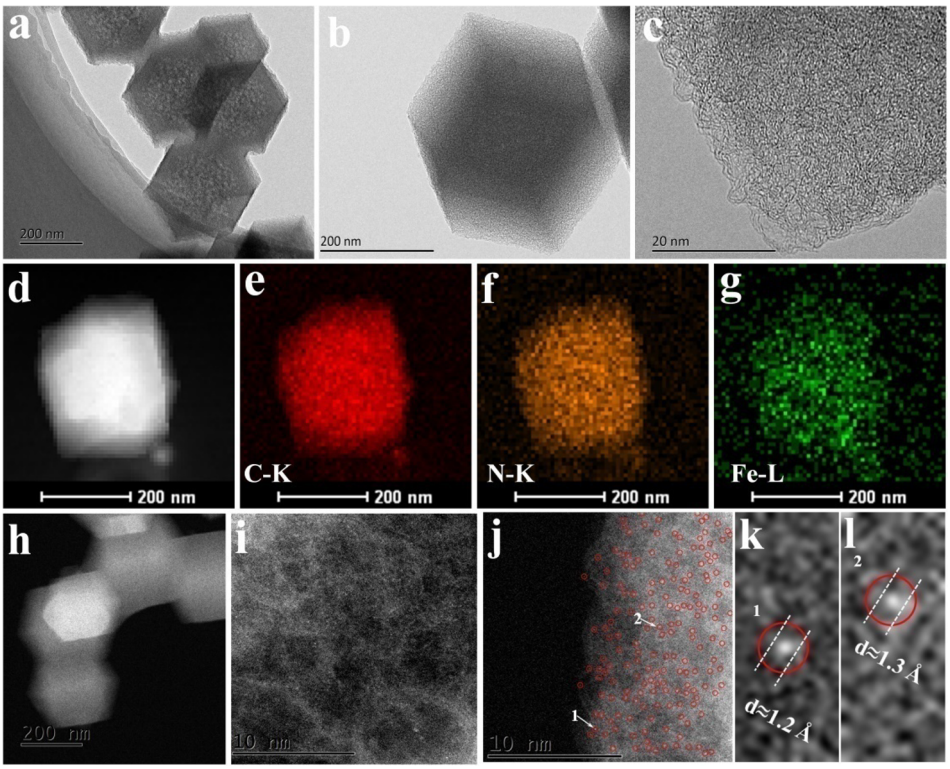

Figure 2. (a–c) TEM images with different magnifications for Fe-N-C-950, (d–g) STEM images and elemental maps of C, N and Fe, and (h–j) STEM and (k, l) corresponding magnified images of Fe-N-C-950, where the white dots are Fe or Zn single atoms.

Synthesis of NC-950 and Fe-N-C-*X* (*X* = Temperature). The powder of ZIF-8 or Fe-ZIF-8 was placed into a quartz boat and then heat-treated at the desired temperature (850–1050 °C, 5 °C min^{-1}) for 1 h under Ar/H_2 (10% H_2) gas in a tube furnace. The pyrolysis products were acid-washed with 1 M HCl solution at 80 °C overnight and then filtered and washed with plenty of deionized water. The final catalysts were obtained by vacuum drying.

Physical Characterization. The dispersion of Fe was characterized by aberration-corrected scanning transmission electron microscopy (Cs-STEM) on a JEOL JEM-ARM200F instrument equipped with a CEOS probe corrector, with a guaranteed resolution of 0.08 nm. The room-temperature ^{57}Fe Mössbauer spectra were recorded using a Topologic 500A spectrometer and a proportional counter. Fe K-edge EXAFS measurements were performed using the 10-ID beamline (MRCAT) from Advanced Photon Sources (APS, Argonne National Laboratory, IL). Fe L-edge and N-edge XANES spectra were measured by collecting the sample drain current (vacuum greater than 10^{-7} Pa) in the total electron yield (TEY) mode on beamline U19 from the National Synchrotron Radiation Laboratory (NSRL, Hefei, People's Republic of China). The in situ Fe K-edge XANES spectra were collected in fluorescence mode at the beamline ISS 8-ID in National Synchrotron Light Source II (NSLS-II) (Brookhaven National Laboratory, NY) at potentials from 0.3 V to 0.9 V vs RHE.

Electrochemical Measurements. The ORR performances were measured in 0.1 M $HClO_4$ at room temperature (~25 °C) on a 750E Bipotentiostat (CH Instruments), and a three-electrode cell was used. A rotating ring–disk electrode (RRDE) coated with catalyst was the working electrode. The catalyst loadings were 0.4 mg cm^{-2} for non-noble-metal catalysts and 40 μg_{Pt} cm^{-2} for Pt/C (20 wt % Pt on Vulcan XC-72 carbon from Johnson Matthey Co.).

RRDE measurements were conducted by linear sweep voltammetry (LSV) from 1.1 to 0 V (5 mV s^{-1}, 1600 rpm), and the ring electrode was held at 1.3 V. The H_2O_2 collection coefficient of the Pt ring was 0.37, on the basis of a $Fe(CN)_6^{4-/3-}$ redox couple measurement. ORR stability was evaluated by an accelerated aging test (ADT) (0.6 and 1.2 V, 0.1 V s^{-1}). After 10000 cycles, the ORR steady-state polarization curves were collected in O_2-saturated electrolyte. Chronoamperometric measurement of Fe-N-C-950 and commercial Pt/C catalysts was also conducted to evaluate the stability.

The turnover frequency (TOF) at 0.8 V is estimated on the basis of the equation

$$\mathrm{TOF} = \frac{J_k N_e}{\omega_{Fe} c_{cat} N_A / M_{Fe}}$$

where J_k represents the kinetic current density (A cm^{-2}), N_e is the electron number per Coulomb 6.24×10^{18}, ω_{Fe} is the active Fe content in Fe-N-C-X, c_{cat} is the catalyst loading, N_A is the Avogadro constant 6.022×10^{23}, and M_{Fe} is the mass per mole of Fe (55.845 g mol^{-1}).

RESULTS AND DISCUSSION

The synthesis of single-atom dispersed Fe-N-C catalysts by a microporous-framework-assisted strategy is illustrated in Figure 1a. $Fe(acac)_3$-incorporated ZIF-8 (denoted as Fe-ZIF-8), which acted as the metal, nitrogen, and carbon sources, was directly pyrolyzed to yield the final product. The microporous character and the isolation effect of Zn are beneficial for forming an Fe–N_x active site structure without a crystalline phase. The crystal structure of final Fe-ZIF-8 and pristine ZIF-8 are compared in

DOI: 10.1021/acscatal.8b00138
ACS Catal. 2018, 8, 2824–2832

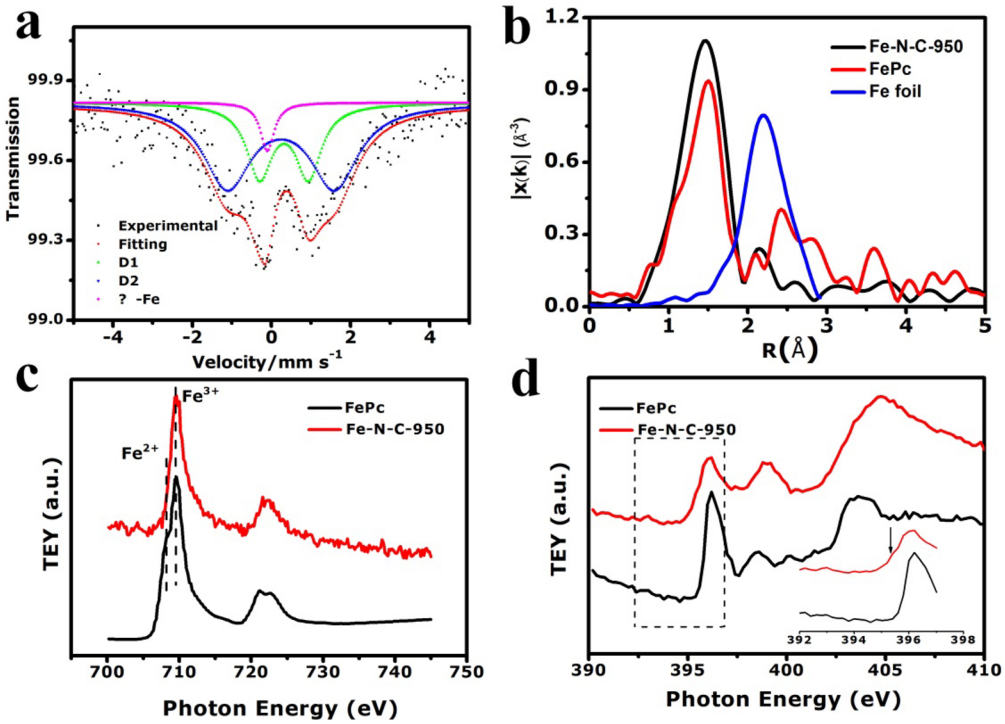

Figure 3. (a) Room-temperature ^{57}Fe Mössbauer spectrum of Fe-N-C-950. (b) Fourier-transformed K-edge EXAFS of Fe for iron phthalocyanine (FePc), iron foil, and Fe-N-C-950. XANES spectra for FePc and Fe-N-C-950 at (c) Fe L-edge recorded in TEY mode and (d) N K-edge (the inset gives an enlarged section).

Figure1b, showing that they share a similar structure. Fourier transform infrared spectroscopy (FTIR, Figure S1) confirmed that Fe is present in the Fe-ZIF-8 through adsorption in the micropores of ZIF-8, rather than partially substituting Zn in the MOFs. The N_2 sorption isotherms and pore structure of Fe-ZIF-8 hardly deviate from those of the pristine ZIF-8 (Figure S2), as the Fe content is ultralow in Fe-ZIF-8 (only 0.137 wt % from ICP analysis). The negligible influence of Fe incorporation in the structure of ZIF-8 can be further observed in their similar rhombdodecahedral morphologies (Figure S3). These results demonstrate the success of the micropore confined strategy toward homogeneously integrating the Fe, N, and C precursors.

Fe-ZIF-8 and pristine ZIF-8 were then subjected to heat treatment (950 °C) under an Ar/H_2 atmosphere for carbonization and Zn removal. From the X-ray diffraction (XRD) patterns, no distinct differences between these two pyrolyzed samples were found, while both amorphous and graphitic carbon characteristic peaks were clearly observed (Figure 1b). The graphitizing degree of the carbonaceous materials was further studied by Raman spectra (Figure S4). A lower I_d/I_g value was obtained on the Fe-N-C samples, and the value significantly decreased with increase in pyrolytic temperature, demonstrating that an ordered carbon structure was formed at higher temperature. Moreover, from the XRD pattern no crystalline iron species were found, suggesting that either Fe is present in the amorphous Fe-N_x coordination or its content is below the detection limit, since the ICP analysis confirmed the existence of Fe. The surface composition was subsequently examined by XPS (Figure 1c and Figure S5), from which typical signals for carbon, nitrogen, and oxygen are observed. The coexistence of three different N species was confirmed by the high-resolution N spectrum. In addition, the total N contents are 2.63−4.97% for Fe-N-C samples, while that for the N−C sample is 6.87%. These results indicated that the N content decreased gradually along with an increase in the pyrolysis temperature (Table S1) due to the different thermal stabilities of different nitrogen species (graphitic N > pyridinic N > pyrrolic N) and the promotion effect of Fe on decomposition of the nitrogen-containing matrix. The non-positive relationship between ORR performance and N content (discussed in a later section) suggests that the N_x-C species was not the dominant active site in our Fe-N-C catalysts. Unfortunately, the XPS signal of iron was so weak that it cannot be further analyzed precisely due to its low content, although the Fe 2p XPS spectra confirmed its presence.

The morphology and pore structure for these samples were probed with electron microscopy and N_2 adsorption−desorption isotherms, respectively. SEM and TEM results (Figure 2 and Figures S6−S9) together demonstrated the rhombododecahedral structure of the unpyrolyzed precursors was retained. No iron nanoparticles were observed in the Fe-N-C-950 sample, and elemental mapping verified the uniform dispersion of Fe atoms on the carbon substrate along with N, implying that iron species must exist at atomic size that are invisible by normal TEM techniques. The formation of the Fe on an atomic scale was confirmed by Cs-STEM measurements. As expected, a large number of bright dots marked with red circles were clearly observed nearly without clusters or small particles. In combination with the ICP result (0.32 wt % Fe and 0.45 wt % Zn detected by ICP), these bright dots were found to correspond to isolated Fe and Zn single atoms.[50,51] This result further verified the success of our micropore-confined strategy for the preferential formation of a single-atom dispersed Fe-N_x configuration. Additionally, the large amount of Zn in the precursor can spatially isolate Fe to suppress its sintering, leading to uniform Fe atomic dispersion. The high surface area with rich nanoporous structure determined from the N_2

DOI: 10.1021/acscatal.8b00138
ACS Catal. 2018, 8, 2824−2832

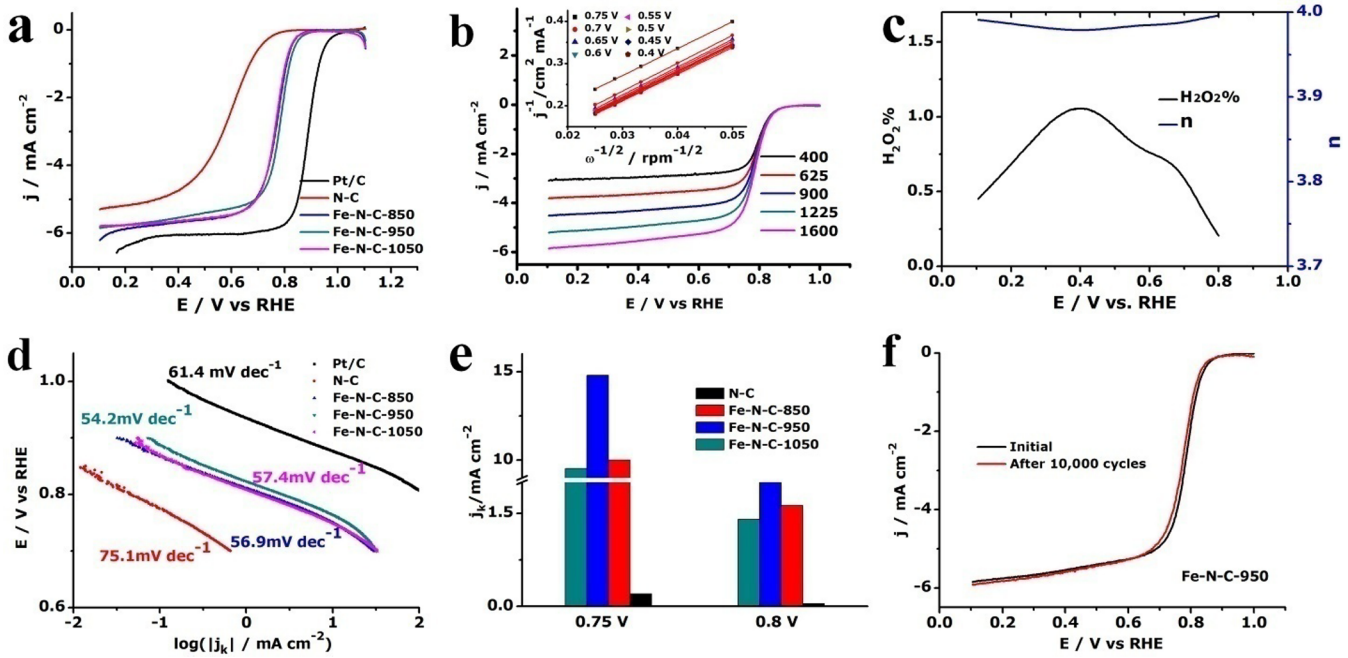

Figure 4. (a) ORR polarization plots in O_2-saturated 0.1 M $HClO_4$ (5 mV s^{-1}, 1600 rpm). (b) LSV curves of Fe-N-C-950 with various rotation rates (the inset gives K-L plots). (c) Electron transfer number and H_2O_2 yield in ORR on Fe-N-C-950 from the RRDE results. (d) Tafel plots of various catalysts. (e) ORR kinetic current density (J_k) on each electrode. (f) ORR polarization plots before and after ADT test.

adsorption−desorption technique (Figure S10) guarantees a rapid mass transfer for electrochemical reactions. These aspects all manifest the advantages of our MOF-templated strategy toward the fabrication of well-dispersed Fe-N-C catalysts.

Due to the fact that the Fe is single-atom dispersed in Fe-N-C, we subsequently resorted to ^{57}Fe Mössbauer spectroscopy and EXAFS analysis to clarify the Fe coordination environment. The ^{57}Fe Mössbauer spectrum of Fe-N-C-950 was fitted with three components: D1 and D2 are commonly assigned to low- and medium-spin states of Fe^{2+} in the square-planar Fe^{2+}-N_4 coordination structure, respectively.[37,52] A singlet near zero velocity represents r-Fe (Figure 3a). Quantitative analysis from the ^{57}Fe Mössbauer spectrum results revealed that the contents of D1, D2, and crystalline iron species were 30.1%, 64.4%, and 5.4%, respectively (Table S2), confirming that the single-atom dispersed Fe−N_4 structure was dominant, which is commonly recognized as the active site for the ORR.[53] Consequently, the high density of Fe−N_4 will guarantee excellent ORR catalytic performance on the Fe-N-C sample. However, some researchers also assigned D2 to the high-spin O_x-Fe^{3+}-N_4 moiety, as some parameters in the Mössbauer spectra are similar.[54] On the basis of XAS experiments, Zitolo et al.[36] claimed that the O_x-Fe-N_4 configuration is responsible for the high activity.

To distinguish the medium-spin Fe^{2+}-N_4 from the high-spin Fe^{3+}-N_4 structure, XAS analyses were conducted. Figure 3b shows the Fourier transformed K-edge EXAFS of Fe for iron phthalocyanine (FePc), iron foil, and Fe-N-C-950. The peak at 2.46 Å (signal from second-shell carbon atom scattering) present for FePc cannot be found in Fe-N-C-950, attributable to incoherent scattering from the disordered carbon. The distinct peak for Fe-N at 1.44 Å was clearly observed in Fe-N-C-950, certifying the presence of Fe-N_x coordination. The weak peaks at 2.1 Å (Fe-Fe scattering signal) indicate the existence of a small quantity of crystalline Fe species, which is consistent with the Mössbauer analysis. According to the fitting parameters (Table S3), the coordination number of Fe-N was 4 with a bond distance of 2.0 Å, while the coordination number of Fe-O was 1 with a bond distance of 1.93 Å, revealing the possible five-coordinated O_x-Fe-N_4 structure. The EXAFS fitting results also confirmed the major presence of Fe-N_4 species (~95%) in the as-synthesized catalyst.

Furthermore, Fe L-edge XANES was employed to analysis the electronic structure of Fe (Figure 3c), as the valence and spin states of 3d transition metals significantly affect the L-edge spectra. The L_3 edge (706−712 eV) involves transitions from $2p_{3/2}$ to 3d states, while the L_2 edge, which ranges from 718 to 726 eV, indicates that the states of Fe transit from $2p_{1/2}$ to 3d. The signals at 706.8 and 709.3 eV in the L_3-edge region can be assigned to Fe^{2+} and Fe^{3+}, respectively. It is clearly observed that Fe^{3+} dominated in the FePc and Fe-N-C catalyst, which is in accordance with the fact that Fe^{2+} in pristine FePc will be oxidized to an Fe^{3+}-like high-spin state on exposure to oxygen.[55] Additionally, a previous report showed a relationship between the area ratios of L_3/L_2 and spin state. The L_3/L_2 ratio for the high-spin configuration is greater than 2/1, and a smaller ratio is achieved for the medium-spin moiety.[56] Miedema et al.[57] calculated the L_3/L_2 ratio of FePc in O_2 to be 3.76, corresponding to 30% Fe^{2+} medium spin + 70% Fe^{3+} high spin. In this work, the L_3/L_2 ratio for FePc is 3, while this value is 3.61 for Fe-N-C-950, further revealing the primary form of the Fe^{3+} high-spin state in Fe-N-C-950. The N K-edge was then studied, in which the intensity of the peak at 395.5 eV increases, which is ascribed to the changes in the N atoms surrounding the Fe ion that supply charge to the oxygen bonding. Considering the major D2 species detected from ^{57}Fe Mössbauer spectroscopy and the dominant Fe^{3+} high-spin state from XAS analysis, it is reasonable to attribute D2 to the high-spin O_x-Fe^{3+}-N_4 rather than the commonly regarded medium-spin Fe^{2+}-N_4. Zitolo et al.[36] claimed that O_2-Fe-N_4 with two different oxygen binding configurations (side-on and end-on) are the active sites instead of low- and medium-spin Fe-N_4. In

DOI: 10.1021/acscatal.8b00138
ACS Catal. 2018, 8, 2824−2832

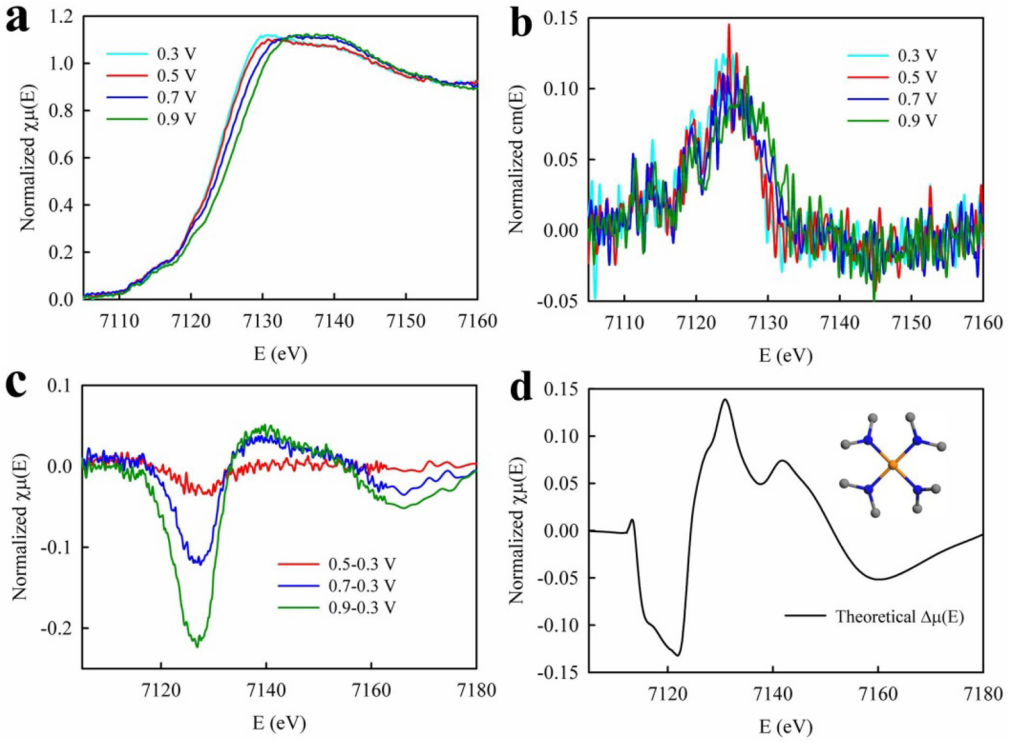

Figure 5. (a) In situ XANES, (b) concomitant first derivatives, and (c) $\Delta\mu$-XANES of the Fe-N-C-950 collected at 0.3−0.9 V on the same electrode in O_2/N_2-saturated electrolyte at 25 °C. (d) Theoretical $\Delta\mu$-XANES obtained by FEF9 calculations with the structural model ($Fe\text{-}N_4\text{-}C_8$) (inset).

addition, the commonly assigned D2 medium-spin $Fe^{2+}\text{-}N_4$ is regarded inactive for the ORR, which means that only a small part of Fe can participate in the ORR. In our catalyst, the D2, high-spin $O_x\text{-}Fe^{3+}\text{-}N_4$ was reported active in the ORR;[58] therefore, outstanding ORR performance was expected for our Fe-N-C catalysts.

The ORR performances of the synthesized catalysts were characterized by the RRDE method. As previous literature[59,60] revealed that the Nafion content would affect the final ORR performance, an optimized Nafion content was used (Figure S11). On the basis of the LSV data in Figure 4a, one can see that the optimized Fe-N-C catalyst outperformed the N−C catalyst and most reported Fe-N-C catalysts (Table S4). The onset and half-wave potentials of Fe-N-C-950 catalyst are 0.92 and 0.78 V, respectively. This promising application of our Fe-N-C catalyst as an alternative to noble-metal catalysts was further confirmed by comparing its ORR performance with that of Pt/C. A four-electron pathway is found to dominate the ORR using Koutecky−Levich plots at 0.4−0.75 V (Figure 4b and Figures S12 and S13), which is in accordance with RRDE results (Figure 4c). In all electrochemical windows, on Fe-N-C-950, the peroxide yield is less than 1.0% (Figure 4c), much lower than those of N-C-950, Fe-N-C-850, and Fe-N-C-1050 samples (Figure S14). The low Tafel slope (54.2 mV dec^{-1}) of Fe-N-C-950 further indicates the superb ORR performance, as shown in Figure 4d, which is even close to that of Pt/C (61.4 mV dec^{-1}). The kinetic current densities (J_k) were maximized for Fe-N-C-950 and decreased in the order of Fe-N-C-950 > Fe-N-C-850 > Fe-N-C-1050, with J_k values of 14.8, 10.1, and 9.5 mA cm^{-2}, respectively, at 0.75 V (Figure 4e). At higher potential (0.8 V), the Fe-N-C-950 catalyst also shows an impressive J_k value: e.g., 2.7 mA cm^{-2}. These data show that Fe-N-C-950 has the highest ORR performance, offering the most positive onset/half-wave potential and largest kinetic current density. Furthermore, excellent electrocatalytic stability is achieved on this catalyst, as confirmed by ADT and chronoamperometric tests. The ADT result revealed that, after 10000 cycles, a 12 mV negative shift in half-wave potential was observed (Figure 4f), similar to that of Pt/C catalyst (10 mV, Figure S15). The current attenuation percentage for the Fe-N-C-950 catalyst within 15000 s is comparable to that of Pt/C catalyst (Figure S16), further verifying the excellent stability of Fe-N-C-950.

The nature of the active site was investigated by the $\Delta\mu$ technique because it is a surface-sensitive spectral subtraction methodology. As shown in Figure 5a, the fingerprint of the square-planar $Fe^{2+}\text{-}N_4$ structure at 7117 eV is not perceptible in the XANES of Fe-N-C-950, thus revealing the nonplanar $Fe\text{-}N_4$ configuration. Increasing the potential resulted in a positive shift in Fe K-edge XANES, indicative of the $Fe^{2+/3+}$ redox transition. The corresponding $\Delta\mu$-XANES spectra exhibited a sinusoidal shape, obviously confirming the nonplanar metal center, with the $Fe^{2+}\text{-}N_4$ oxidized to a pentacoordinate $O_x\text{-}Fe^{3+}\text{-}N_4$ environment at high potentials. Furthermore, with an increase in the potential, the amplitude of the primary peak at 7216 eV increased and reached a maximum at 0.9 V, revealing that the coverage of $Fe\text{-}N_4$ by the oxygenated species increased until 0.9 V. Considering the ex situ XAS analysis, D2 in this work is high-spin $O_x\text{-}Fe^{3+}\text{-}N_4$; therefore, the in situ XANES spectra and $\Delta\mu$ spectra revealed that the pristine high-spin $O_x\text{-}Fe^{3+}\text{-}N_4$ was reduced to $HO\text{-}*Fe^{(2+)}\text{-}N_4$, which served as an active site for the ORR, at potentials below the Fe^{2+}/Fe^{3+} redox potential, according to the equation

$$O_x\text{-}Fe^{3+}\text{-}N_4 + e^- \leftrightarrow HO\text{-}*Fe^{(2+)}\text{-}N_4 \quad (1)$$

This phenomenon was previously confirmed by using density functional theory (DFT) calculations. Forming a $Fe\text{-}O_x$ structure would gain a free energy of 2.52 eV due to the

DOI: 10.1021/acscatal.8b00138
ACS Catal. 2018, 8, 2824−2832

strong adsorption of O, and the formation of OH-Fe^{2+}-N_4 process could promote the reaction by lowering the activation barrier by 0.48 eV.[51] Additionally, Holby et al.[61] also demonstrated the spontaneously formed *OH resulting in a new active site rather than poisoning the site and this new site theoretically has higher ORR activity. The structural model used in the simulation of theoretical $\Delta\mu$ spectra essentially represents FeN_4C_8 with an axially bonded oxygen atom (Figure 5d), which will switch to nonplanar Fe^{2+}-N_4 below the Fe^{2+}/Fe^{3+} redox potential as an ORR active site. Supposing that D1 and D2 contribute equally to the whole ORR activity, the average TOF is calculated to be 1.27 e s^{-1} $sites^{-1}$, much higher than the already known TOF result for D1 of 0.33 e s^{-1} $sites^{-1}$ as reported by Zitolo et al.,[36] suggesting the dominant contribution of D2 to ORR activity. In addition, the estimated TOF of D2 is approximately 1.71 e s^{-1} $sites^{-1}$, which greatly exceeds most of the reported NPMCs (Table S5). The much higher TOF of D2 in comparison with D1 can explain the enhanced ORR activity on our catalyst, although its Fe content is rather low (only 0.32 wt %).

CONCLUSION

In summary, we describe a single-metal dispersed Fe-N-C electrocatalyst fabricated by a microporous MOF-assisted strategy and demonstrated its superior ORR activity using the RRDE method. Further structural analysis revealed that D2, commonly attributed to medium-spin Fe^{2+}-N_4, is assigned to the high-spin O_x-Fe^{3+}-N_4 moiety from the five-coordinated feature, high Fe^{3+}/Fe^{2+} ratio, and L_3/L_2 area ratio. In situ XANES demonstrated the O_x-Fe^{3+}-N_4 undergoes an Fe^{3+}/Fe^{2+} transition with a decrease in the potential and the active site nonplanar HO-*$Fe^{(2+)}$-N_4 was formed in situ below the Fe^{2+}/Fe^{3+} redox potential. The in situ freshly reduced HO-*$Fe^{(2+)}$-N_4 active site has an ultrahigh TOF of 1.71 e s^{-1} $sites^{-1}$; thus, excellent ORR performance was achieved with our pyrolyzed Fe-N-C catalyst.

ASSOCIATED CONTENT

Supporting Information

The Supporting Information is available free of charge on the ACS Publications website at DOI: 10.1021/acscatal.8b00138.

Details of physical characterization methods and physical and electrochemical measurements (PDF)

AUTHOR INFORMATION

Corresponding Authors

*E-mail for J.G.: gejj@ciac.ac.cn.
*E-mail for Q.H.: qghe@zju.edu.cn.
*E-mail for W.X.: xingwei@ciac.ac.cn.

ORCID

Yang Hou: 0000-0001-9795-8503
Jingkun Li: 0000-0003-1699-3089
Qingying Jia: 0000-0002-4005-8894
Zheng Jiang: 0000-0002-0132-0319
Wei Xing: 0000-0003-2841-7206

Notes

The authors declare no competing financial interest.

ACKNOWLEDGMENTS

The work was supported by the National Natural Science Foundation of China (21633008, 21433003, U1601211, 21733004), National Science and Technology Major Project (2016YFB0101202), Jilin Province Science and Technology Development Program (20150101066JC, 20160622037JC, 20170203003SF, 20170520150JH), Hundred Talents Program of Chinese Academy of Sciences, and the Recruitment Program of Foreign Experts (WQ20122200077). Q.J. acknowledges the use of ISS 8-ID of the NSLS II was supported by the National Synchrotron Light Source (NSLS) II, Brookhaven National Laboratory, under U.S. DOE Contract No. DE-SC0012704. Brookhaven National Laboratory was supported by the U.S. Department of Energy, Office of Science, Office of Basic Energy Sciences, under Contract No. DE-AC02-98CH10886.

REFERENCES

(1) Steele, B. C. H.; Heinzel, A. Materials for fuel-cell technologies. *Nature* **2001**, *414*, 345−352.
(2) Debe, M. K. Electrocatalyst approaches and challenges for automotive fuel cells. *Nature* **2012**, *486*, 43−51.
(3) Gong, K. P.; Du, F.; Xia, Z. H.; Durstock, M.; Dai, L. M. Nitrogen-Doped Carbon Nanotube Arrays with High Electrocatalytic Activity for Oxygen Reduction. *Science* **2009**, *323*, 760−764.
(4) Lefevre, M.; Proietti, E.; Jaouen, F.; Dodelet, J. P. Iron-Based Catalysts with Improved Oxygen Reduction Activity in Polymer Electrolyte Fuel Cells. *Science* **2009**, *324*, 71−74.
(5) Jasinski, R. New Fuel Cell Cathode Catalyst. *Nature* **1964**, *201*, 1212−1213.
(6) Wiesener, K.; Ohms, D.; Neumann, V.; Franke, R. N-4 Macrocycles as Electrocatalysts for the Cathodic Reduction of Oxygen. *Mater. Chem. Phys.* **1989**, *22*, 457−475.
(7) Gupta, S.; Tryk, D.; Bae, I.; Aldred, W.; Yeager, E. Heat-Treated Polyacrylonitrile-Based Catalysts for Oxygen Electroreduction. *J. Appl. Electrochem.* **1989**, *19*, 19−27.
(8) Faubert, G.; Lalande, G.; Cote, R.; Guay, D.; Dodelet, J. P.; Weng, L. T.; Bertrand, P.; Denes, G. Heat-treated iron and cobalt tetraphenylporphyrins adsorbed on carbon black: Physical characterization and catalytic properties of these materials for the reduction of oxygen in polymer electrolyte fuel cells. *Electrochim. Acta* **1996**, *41*, 1689−1701.
(9) Wu, G.; More, K. L.; Johnston, C. M.; Zelenay, P. High-Performance Electrocatalysts for Oxygen Reduction Derived from Polyaniline, Iron, and Cobalt. *Science* **2011**, *332*, 443−447.
(10) Jaouen, F.; Marcotte, S.; Dodelet, J. P.; Lindbergh, G. Oxygen reduction catalysts for polymer electrolyte fuel cells from the pyrolysis of iron acetate adsorbed on various carbon supports. *J. Phys. Chem. B* **2003**, *107*, 1376−1386.
(11) Chung, H. T.; Johnston, C. M.; Artyushkova, K.; Ferrandon, M.; Myers, D. J.; Zelenay, P. Cyanamide-derived non-precious metal catalyst for oxygen reduction. *Electrochem. Commun.* **2010**, *12*, 1792−1795.
(12) Wu, G.; Mack, N. H.; Gao, W.; Ma, S. G.; Zhong, R. Q.; Han, J. T.; Baldwin, J. K.; Zelenay, P. Nitrogen Doped Graphene-Rich Catalysts Derived from Heteroatom Polymers for Oxygen Reduction in Nonaqueous Lithium-O-2 Battery Cathodes. *ACS Nano* **2012**, *6*, 9764−9776.
(13) Chung, H. T.; Won, J. H.; Zelenay, P. Active and stable carbon nanotube/nanoparticle composite electrocatalyst for oxygen reduction. *Nat. Commun.* **2013**, *4*, 1922−1926.
(14) Chung, H. T.; Wu, G.; Li, Q.; Zelenay, P. Role of two carbon phases in oxygen reduction reaction on the Co-PPy-C catalyst. *Int. J. Hydrogen Energy* **2014**, *39*, 15887−15893.
(15) Wen, Z. H.; Ci, S. Q.; Hou, Y.; Chen, J. H. Facile One-Pot, One-Step Synthesis of a Carbon Nanoarchitecture for an Advanced Multifunctonal Electrocatalyst. *Angew. Chem., Int. Ed.* **2014**, *53*, 6496−6500.
(16) Wang, Q.; Zhou, Z. Y.; Lai, Y. J.; You, Y.; Liu, J. G.; Wu, X. L.; Terefe, E.; Chen, C.; Song, L.; Rauf, M.; Tian, N.; Sun, S. G. Phenylenediamine-Based FeNx/C Catalyst with High Activity for

DOI: 10.1021/acscatal.8b00138
ACS Catal. 2018, 8, 2824−2832

Oxygen Reduction in Acid Medium and Its Active-Site Probing. *J. Am. Chem. Soc.* **2014**, *136*, 10882−10885.
(17) Xiao, M. L.; Zhu, J. B.; Feng, L. G.; Liu, C. P.; Xing, W. Meso/Macroporous Nitrogen-Doped Carbon Architectures with Iron Carbide Encapsulated in Graphitic Layers as an Efficient and Robust Catalyst for the Oxygen Reduction Reaction in Both Acidic and Alkaline Solutions. *Adv. Mater.* **2015**, *27*, 2521−2527.
(18) Zhu, J. B.; Xiao, M. L.; Liu, C. P.; Ge, J. J.; St-Pierre, J.; Xing, W. Growth mechanism and active site probing of Fe3C@N-doped carbon nanotubes/C catalysts: guidance for building highly efficient oxygen reduction electrocatalysts. *J. Mater. Chem. A* **2015**, *3*, 21451−21459.
(19) Yang, Z. K.; Lin, L.; Xu, A. W. 2D Nanoporous Fe− N/C Nanosheets as Highly Efficient Non-Platinum Electrocatalysts for Oxygen Reduction Reaction in Zn-Air Battery. *Small* **2016**, *12*, 5710−5719.
(20) Yang, Z. K.; Zhao, Z.-W.; Liang, K.; Zhou, X.; Shen, C.-C.; Liu, Y.-N.; Wang, X.; Xu, A.-W. Synthesis of nanoporous structured iron carbide/Fe−N−carbon composites for efficient oxygen reduction reaction in Zn−air batteries. *J. Mater. Chem. A* **2016**, *4*, 19037−19044.
(21) Li, Z. L.; Li, G. L.; Jiang, L. H.; Li, J. L.; Sun, G. Q.; Xia, C. G.; Li, F. W. Ionic Liquids as Precursors for Efficient Mesoporous Iron-Nitrogen-Doped Oxygen Reduction Electrocatalysts. *Angew. Chem., Int. Ed.* **2015**, *54*, 1494−1498.
(22) Niu, W. H.; Li, L. G.; Liu, X. J.; Wang, N.; Liu, J.; Zhou, W. J.; Tang, Z. H.; Chen, S. W. Mesoporous N-Doped Carbons Prepared with Thermally Removable Nanoparticle Templates: An Efficient Electrocatalyst for Oxygen Reduction Reaction. *J. Am. Chem. Soc.* **2015**, *137*, 5555−5562.
(23) Sa, Y. J.; Seo, D. J.; Woo, J.; Lim, J. T.; Cheon, J. Y.; Yang, S. Y.; Lee, J. M.; Kang, D.; Shin, T. J.; Shin, H. S.; Jeong, H. Y.; Kim, C. S.; Kim, M. G.; Kim, T. Y.; Joo, S. H. A General Approach to Preferential Formation of Active Fe-N-x Sites in Fe-N/C Electrocatalysts for Efficient Oxygen Reduction Reaction. *J. Am. Chem. Soc.* **2016**, *138*, 15046−15056.
(24) Meng, F. L.; Wang, Z. L.; Zhong, H. X.; Wang, J.; Yan, J. M.; Zhang, X. B. Reactive Multifunctional Template-Induced Preparation of Fe-N-Doped Mesoporous Carbon Microspheres Towards Highly Efficient Electrocatalysts for Oxygen Reduction. *Adv. Mater.* **2016**, *28*, 7948−7955.
(25) Shang, L.; Yu, H. J.; Huang, X.; Bian, T.; Shi, R.; Zhao, Y. F.; Waterhouse, G. I. N.; Wu, L. Z.; Tung, C. H.; Zhang, T. R. Well-Dispersed ZIF-Derived Co,N-Co-doped Carbon Nanoframes through Mesoporous-Silica-Protected Calcination as Efficient Oxygen Reduction Electrocatalysts. *Adv. Mater.* **2016**, *28*, 1668−1674.
(26) Yin, P. Q.; Yao, T.; Wu, Y.; Zheng, L. R.; Lin, Y.; Liu, W.; Ju, H. X.; Zhu, J. F.; Hong, X.; Deng, Z. X.; Zhou, G.; Wei, S. Q.; Li, Y. D. Single Cobalt Atoms with Precise N-Coordination as Superior Oxygen Reduction Reaction Catalysts. *Angew. Chem., Int. Ed.* **2016**, *55*, 10800−10805.
(27) Kobayashi, M.; Niwa, H.; Saito, M.; Harada, Y.; Oshima, M.; Ofuchi, H.; Terakura, K.; Ikeda, T.; Koshigoe, Y.; Ozaki, J.; Miyata, S. Indirect contribution of transition metal towards oxygen reduction reaction activity in iron phthalocyanine-based carbon catalysts for polymer electrolyte fuel cells. *Electrochim. Acta* **2012**, *74*, 254−259.
(28) Kobayashi, M.; Niwa, H.; Harada, Y.; Horiba, K.; Oshima, M.; Ofuchi, H.; Terakura, K.; Ikeda, T.; Koshigoe, Y.; Ozaki, J.; Miyata, S.; Ueda, S.; Yamashita, Y.; Yoshikawa, H.; Kobayashi, K. Role of residual transition-metal atoms in oxygen reduction reaction in cobalt phthalocyanine-based carbon cathode catalysts for polymer electrolyte fuel cell. *J. Power Sources* **2011**, *196*, 8346−8351.
(29) Szakacs, C. E.; Lefevre, M.; Kramm, U. I.; Dodelet, J. P.; Vidal, F. A density functional theory study of catalytic sites for oxygen reduction in Fe/N/C catalysts used in H-2/O-2 fuel cells. *Phys. Chem. Chem. Phys.* **2014**, *16*, 13654−13661.
(30) Masa, J.; Xia, W.; Muhler, M.; Schuhmann, W. On the Role of Metals in Nitrogen-Doped Carbon Electrocatalysts for Oxygen Reduction. *Angew. Chem., Int. Ed.* **2015**, *54*, 10102−10120.
(31) Matter, P. H.; Wang, E.; Arias, M.; Biddinger, E. J.; Ozkan, U. S. Oxygen reduction reaction catalysts prepared from acetonitrile pyrolysis over alumina-supported metal particles. *J. Phys. Chem. B* **2006**, *110*, 18374−18384.
(32) Choi, C. H.; Lim, H. K.; Chung, M. W.; Park, J. C.; Shin, H.; Kim, H.; Woo, S. I. Long-Range Electron Transfer over Graphene-Based Catalyst for High-Performing Oxygen Reduction Reactions: Importance of Size, N-doping, and Metallic Impurities. *J. Am. Chem. Soc.* **2014**, *136*, 9070−9077.
(33) Maldonado, S.; Stevenson, K. J. Influence of nitrogen doping on oxygen reduction electrocatalysis at carbon nanofiber electrodes. *J. Phys. Chem. B* **2005**, *109*, 4707−4716.
(34) Schulenburg, H.; Stankov, S.; Schunemann, V.; Radnik, J.; Dorbandt, I.; Fiechter, S.; Bogdanoff, P.; Tributsch, H. Catalysts for the oxygen reduction from heat-treated iron(III) tetramethoxyphenylporphyrin chloride: Structure and stability of active sites. *J. Phys. Chem. B* **2003**, *107*, 9034−9041.
(35) Bouwkamp-Wijnoltz, A. L.; Visscher, W.; van Veen, J. A. R.; Boellaard, E.; van der Kraan, A. M.; Tang, S. C. On active-site heterogeneity in pyrolyzed carbon-supported iron porphyrin catalysts for the electrochemical reduction of oxygen: An in situ Mossbauer study. *J. Phys. Chem. B* **2002**, *106*, 12993−13001.
(36) Zitolo, A.; Goellner, V.; Armel, V.; Sougrati, M. T.; Mineva, T.; Stievano, L.; Fonda, E.; Jaouen, F. Identification of catalytic sites for oxygen reduction in iron- and nitrogen-doped graphene materials. *Nat. Mater.* **2015**, *14*, 937−944.
(37) Kramm, U. I.; Herranz, J.; Larouche, N.; Arruda, T. M.; Lefevre, M.; Jaouen, F.; Bogdanoff, P.; Fiechter, S.; Abs-Wurmbach, I.; Mukerjee, S.; Dodelet, J. P. Structure of the catalytic sites in Fe/N/C-catalysts for O-2-reduction in PEM fuel cells. *Phys. Chem. Chem. Phys.* **2012**, *14*, 11673−11688.
(38) Holby, E. F.; Wu, G.; Zelenay, P.; Taylor, C. D. Structure of Fe-N-x-C Defects in Oxygen Reduction Reaction Catalysts from First-Principles Modeling. *J. Phys. Chem. C* **2014**, *118*, 14388−14393.
(39) Lin, L.; Zhu, Q.; Xu, A.-W. Noble-metal-free Fe−N/C catalyst for highly efficient oxygen reduction reaction under both alkaline and acidic conditions. *J. Am. Chem. Soc.* **2014**, *136*, 11027−11033.
(40) Lin, L.; Yang, Z. K.; Jiang, Y.-F.; Xu, A.-W. Nonprecious Bimetallic (Fe, Mo)−N/C Catalyst for Efficient Oxygen Reduction Reaction. *ACS Catal.* **2016**, *6*, 4449−4454.
(41) Proietti, E.; Dodelet, J. P. Ballmilling of Carbon Supports to Enhance the Performance of Fe-based Electrocatalysts for Oxygen Reduction in PEM Fuel Cells. *ECS Trans.* **2008**, *16*, 393−404.
(42) Lefevre, M.; Dodelet, J. P. Fe-based electrocatalysts made with microporous pristine carbon black supports for the reduction of oxygen in PEM fuel cells. *Electrochim. Acta* **2008**, *53*, 8269−8276.
(43) Charreteur, F.; Jaouen, F.; Ruggeri, S.; Dodelet, J. P. Fe/N/C non-precious catalysts for PEM fuel cells: Influence of the structural parameters of pristine commercial carbon blacks on their activity for oxygen reduction. *Electrochim. Acta* **2008**, *53*, 2925−2938.
(44) Jaouen, F.; Charreteur, F.; Dodelet, J. P. Fe-based catalysts for oxygen reduction in PEMFCs - Importance of the disordered phase of the carbon support. *J. Electrochem. Soc.* **2006**, *153*, A689−A698.
(45) Tian, J.; Birry, L.; Jaouen, F.; Dodelet, J. P. Fe-based catalysts for oxygen reduction in proton exchange membrane fuel cells with cyanamide as nitrogen precursor and/or pore-filler. *Electrochim. Acta* **2011**, *56*, 3276−3285.
(46) Deng, D.; Yu, L.; Chen, X.; Wang, G.; Jin, L.; Pan, X.; Deng, J.; Sun, G.; Bao, X. Iron encapsulated within pod-like carbon nanotubes for oxygen reduction reaction. *Angew. Chem., Int. Ed.* **2013**, *52*, 371−375.
(47) Liang, H.-W.; Wei, W.; Wu, Z.-S.; Feng, X.; Müllen, K. Mesoporous metal−nitrogen-doped carbon electrocatalysts for highly efficient oxygen reduction reaction. *J. Am. Chem. Soc.* **2013**, *135*, 16002−16005.
(48) Zhang, J.; Zhao, Z.; Xia, Z.; Dai, L. A metal-free bifunctional electrocatalyst for oxygen reduction and oxygen evolution reactions. *Nat. Nanotechnol.* **2015**, *10*, 444−452.
(49) Jaouen, F.; Herranz, J.; Lefevre, M.; Dodelet, J.-P.; Kramm, U. I.; Herrmann, I.; Bogdanoff, P.; Maruyama, J.; Nagaoka, T.; Garsuch, A. Cross-laboratory experimental study of non-noble-metal electro-

DOI: 10.1021/acscatal.8b00138
ACS Catal. 2018, 8, 2824−2832

catalysts for the oxygen reduction reaction. *ACS Appl. Mater. Interfaces* **2009**, *1*, 1623−1639.
(50) Fei, H.; Dong, J.; Arellano-Jiménez, M. J.; Ye, G.; Dong Kim, N.; Samuel, E. L. G.; Peng, Z.; Zhu, Z.; Qin, F.; Bao, J.; Yacaman, M. J.; Ajayan, P. M.; Chen, D.; Tour, J. M. Atomic cobalt on nitrogen-doped graphene for hydrogen generation. *Nat. Commun.* **2015**, *6*, 8668.
(51) Chen, X.; Yu, L.; Wang, S.; Deng, D.; Bao, X. Highly active and stable single iron site confined in graphene nanosheets for oxygen reduction reaction. *Nano Energy* **2017**, *32*, 353−358.
(52) Kramm, U. I.; Lefevre, M.; Larouche, N.; Schmeisser, D.; Dodelet, J. P. Correlations between mass activity and physicochemical properties of Fe/N/C catalysts for the ORR in PEM fuel cell via 57Fe Mossbauer spectroscopy and other techniques. *J. Am. Chem. Soc.* **2014**, *136*, 978−85.
(53) Miller, H. A.; Bellini, M.; Oberhauser, W.; Deng, X.; Chen, H. Q.; He, Q. G.; Passaponti, M.; Innocenti, M.; Yang, R. O.; Sun, F. F.; Jiang, Z.; Vizza, F. Heat treated carbon supported iron(II)-phthalocyanine oxygen reduction catalysts: elucidation of the structure-activity relationship using X-ray absorption spectroscopy. *Phys. Chem. Chem. Phys.* **2016**, *18*, 33142−33151.
(54) Schulenburg, H.; Stankov, S.; Schünemann, V.; Radnik, J.; Dorbandt, I.; Fiechter, S.; Bogdanoff, P.; Tributsch, H. Catalysts for the Oxygen Reduction from Heat-Treated Iron(III) Tetramethoxyphenylporphyrin Chloride: Structure and Stability of Active Sites. *J. Phys. Chem. B* **2003**, *107*, 9034−9041.
(55) Cook, P. L.; Liu, X. S.; Yang, W. L.; Himpsel, F. J. X-ray absorption spectroscopy of biomimetic dye molecules for solar cells. *J. Chem. Phys.* **2009**, *131*, 194701.
(56) Thole, B. T.; Vanderlaan, G.; Butler, P. H. Spin-Mixed Ground-State of Fe Phthalocyanine and the Temperature-Dependent Branching Ratio in X-Ray Absorption-Spectroscopy. *Chem. Phys. Lett.* **1988**, *149*, 295−299.
(57) Miedema, P. S.; van Schooneveld, M. M.; Bogerd, R.; Rocha, T. C. R.; Havecker, M.; Knop-Gericke, A.; de Groott, F. M. F. Oxygen Binding to Cobalt and Iron Phthalocyanines As Determined from in Situ X-ray Absorption Spectroscopy. *J. Phys. Chem. C* **2011**, *115*, 25422−25428.
(58) Li, J.; Ghoshal, S.; Liang, W.; Sougrati, M.-T.; Jaouen, F.; Halevi, B.; McKinney, S.; McCool, G.; Ma, C.; Yuan, X.; Ma, Z.-F.; Mukerjee, S.; Jia, Q. Structural and mechanistic basis for the high activity of Fe-N-C catalysts toward oxygen reduction. *Energy Environ. Sci.* **2016**, *9*, 2418−2432.
(59) Chlistunoff, J.; Sansinena, J. M. Nafion Induced Surface Confinement of Oxygen in Carbon-Supported Oxygen Reduction Catalysts. *J. Phys. Chem. C* **2016**, *120*, 28038−28048.
(60) Chlistunoff, J.; Sansinena, J. M. On the use of Nafion (R) in electrochemical studies of carbon supported oxygen reduction catalysts in aqueous media. *J. Electroanal. Chem.* **2016**, *780*, 134−146.
(61) Holby, E. F.; Taylor, C. D. Activity of N-coordinated multi-metal-atom active site structures for Pt-free oxygen reduction reaction catalysis: Role of *OH ligands. *Sci. Rep.* **2015**, *5*, 9286.

DOI: 10.1021/acscatal.8b00138
ACS Catal. 2018, 8, 2824−2832